**J. Cent. South Univ.** (2015) 22: 4844−4855
**DOI:** 10.1007/s11771-015-3036-2

Springer

# A DEM investigation on simple shear behavior of dense granular assemblies

SHI Dan-da(史旦达)[1], XUE Jian-feng(薛剑峰)[2], ZHAO Zhen-ying(赵振营)[1], SHI Ji-yu(史跻宇)[3]

1. School of Ocean Science and Engineering, Shanghai Maritime University, Shanghai 201306, China;
2. School of Engineering and Information Technology, Federation University Australia, Churchill 3842, VIC, Australia;
3. Jiangsu Zhongshe Engineering Consultancy Group, Wuxi 214072, China



**Abstract:** A micromechanical investigation on simple shear behavior of dense granular assemblies was carried out by discrete element method. Three series of numerical tests were performed to examine the effects of initial porosity, vertical stress and particle shape on simple shear behavior of the samples, respectively. It was found that during simple shear the directions of principal stress and principal strain increment rotate differently with shear strain level. The non-coaxiality between the two directions decreases with strain level and may greatly affect the shear behavior of the assemblies, especially their peak friction angles. The numerical modelling also reveals that the rotation of the principal direction of fabric anisotropy lags behind that of the major principal stress direction during simple shear, which is described as fabric hyteresis effect. The degrees of fabric and interparticle contact force anisotropies increase as particle angularity increases, whereas the orientations of these anisotropies have not been significantly influenced by particle shape. An extended stress–dilatancy relationship based on ROWE-DAVIS framework was proposed to consider the non-coaxiality effect under principal stress rotation. The model was validated by present numerical results as well as some published physical test and numerical modelled data.

**Key words:** simple shear; non-coaxiality; fabric anisotropy; shear strength; discrete element method

## 1 Introduction

Behavior of soil under simple shear is often required for analyzing the stability of many geotechnical structures, such as stability of soil slopes and embankments on soft soils. Simple shear test has been widely used to study the stress−strain−strength relationship of soils under simple shear. The major advantage of simple shear tests over direct shear tests is the uniform stress and deformation distributions within the soil samples [1]. Since the first simple shear apparatus (SSA) was invented by Swedish Geotechnical Institute [2], many researchers have examined the drained and undrained simple shear behaviors of sands and clays by different typed SSAs [3−5]. Different from triaxial compression and plane strain tests, one of the distinctive features of simple shear tests is the rotation of principal stress direction during shear. Although the overall stress and strain can be directly measured from the boundaries of SSA, the main shortcoming of conventional simple shear tests is that the internal stress and strain, as well as the soil fabric, cannot be easily captured even by advanced measurement techniques. To overcome this deficiency, some ideal granular materials such as aluminum rods and photoelastic substances have been adopted in simple shear tests [6−7], but the application is limited as it is time-consuming to prepare samples and expensive to run the tests.

Many researchers used discrete element method (DEM) to simulate laboratory tests including simple shear, to investigate the macroscopic behavior of granular assemblies on micro scale. LIU and LU [8] investigated the simple shear behavior of an assembly of two-dimensional aluminum rods using DEM, and a stress-fabric relationship was suggested by analyzing fabric anisotropy during shear. THORNTON and ZHANG [9] performed simple shear simulations using DEM to study the non-coaxiality effect, i.e. the deviation between the directions of principal stress and principal strain increment, and the influences of initial stress ratio on non-coaxiality were intensively investigated. SHEN et al [10] examined the effects of boundary conditions on simple shear behavior of granular systems using DEM. In the analysis the authors simulated the simple shear in laminar and rigid boxes to compare the effect of rigid

**Foundation item:** Projects(50909057, 51208294, 41372319) supported by the National Natural Science Foundation of China; Project(15ZZ081) supported by Innovation Program of Shanghai Municipal Education Commission, China; Project(20131129) supported by Innovation Program of Shanghai Postgraduate Education, China
**Received date:** 2014−10−29; **Accepted date:** 2015−01−30
**Corresponding author:** SHI Dan-da, PhD, Associate Professor; Tel: +86−21−38282503; E-mail: ddshi@shmtu.edu.cn

and flexible boundaries. It was found that the strain distribution within the samples is affected by the rigidity of the walls. Recently, QIAN et al [11] explored the relationship between shear strength anisotropy and fabric anisotropy under simple shear. The effects of non-coaxiality on the stress-dilatancy behavior of numerical samples were analytically discussed. However, the published results are mostly achieved from DEM simulations using circular particles, and few attempts have been made on the investigations of particle shape factor. Meanwhile, the non-coaxial flow rules and the corresponding macro-micro relationships due to principal stress rotation also need to be further studied.

In this work, three series of simple shear tests were simulated using PFC$^{2D}$ on both circular and non-circular particle samples to study the effects of initial porosity, vertical stress and particle shape on the simple shear behavior. An extended stress–dilatancy relationship under simple shear condition on the basis of ROWE-DAVIS framework was proposed to consider the non-coaxiality effect. Stress-induced fabric and contact force anisotropies were primarily examined, and the fabric hyteresis effect between the orientation of fabric anisotropy and the major principal stress direction was explored. Finally, an empirical stress–force–fabric relationship based on ROTHENBURG and BATHURST's equation was suggested to consider the fabric hyteresis effect induced by principal stress rotation.

## 2 Numerical sampling

### 2.1 DEM simulated simple shear tests

Simple shear tests were simulated in PFC$^{2D}$ on polydisperse granular materials with particle diameter ranging from 0.15 mm to 0.2 mm. Both circular and non-circular particle elements were introduced in the present simulations. A linear contact-stiffness model with Coulomb sliding criterion was adopted to describe the interaction between particles. Local damping mechanism was introduced to ensure the quasi-static equilibrium of granular assemblies. The micromechanical parameters of interparticle contact model were calibrated on the basis of a drained triaxial compression test on dense Fujian standard sand [12], which is a standard sand used in China by most researchers. The material parameters used for DEM analyses are listed in Table 1.

The particles were encased in a simple shear box simulated with four rigid walls as illustrated in Fig. 1(a), in which the solid lines indicate the initial position of the walls and the dashed lines show the position of walls after shearing. The size of the two-dimensional sample is 5 mm×5 mm. After the sample being generated, isotropic consolidation stress was applied to the sample by

**Table 1** Material parameters for DEM simulations

| Parameter | Value |
|---|---|
| Normal contact stiffness between particles/(N·m$^{-1}$) | $2\times10^8$ |
| Tangential contact stiffness between particles/(N·m$^{-1}$) | $1\times10^8$ |
| Local damping coefficient | 0.7 |
| Friction coefficient between particles | 0.5 |
| Particle density/(kg·m$^{-3}$) | 2650 |
| Normal contact stiffness between particle and wall/(N·m$^{-1}$) | $4\times10^8$ |
| Tangential contact stiffness between particle and wall/(N·m$^{-1}$) | $2\times10^8$ |
| Friction coefficient between particle and wall | 0.5 |

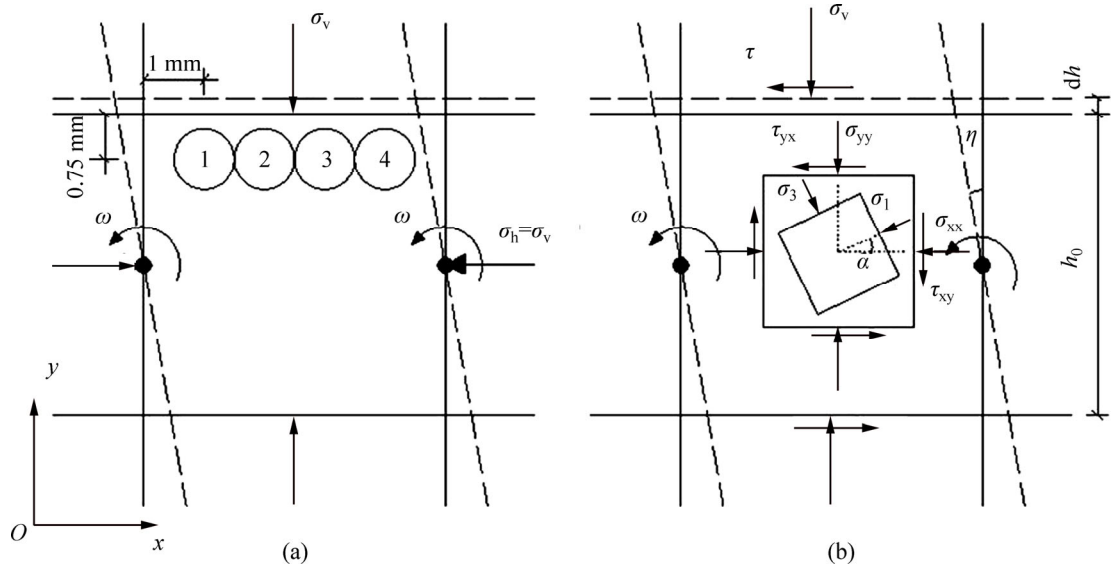


**Fig. 1** Scheme for DEM simulations of simple shear: (a) Sample boundaries and measurement circles; (b) Sample deformation and internal stress state

servo-control mechanism in PFC$^{2D}$. Then, the two lateral walls were rotated about their centroids with an angular velocity of $8.0\times10^{-5}$ rad/s, which is a very low velocity to minimize the dynamic effect between the elements. The bottom wall was fixed and the samples were sheared at constant vertical stresses.

Figure 1(b) presents the schematic diagram of simple shear deformation and the stress state of soil element within the sample. Since there is no lateral normal strain ($\varepsilon_{xx}$) in simple shear, the shear strain ($\gamma$) and volumetric strain ($\varepsilon_v$) can be calculated as

$$\gamma = \tan\eta \tag{1}$$

$$\varepsilon_v = \varepsilon_{xx} + \varepsilon_{yy} = \varepsilon_{yy} = \frac{dh}{h_0} \tag{2}$$

where $\eta$ is the rotational angle of the lateral walls, and $\varepsilon_{yy}$ is the vertical normal strain component, which is the ratio between the change of height ($dh$) and the initial height of the sample ($h_0$). The volumetric strain $\varepsilon_v$ is positive for contraction and negative for dilation.

As indicated by QIAN et al [11], the distribution of shear stress at the top boundary in simple shear sample is generally non-uniform. To study this, four zones with a diameter of 1 mm each were assigned near the top plate to measure the internal stress and strain increment, as shown in Fig. 1(a). The average values of stress components ($\tau_{xy}$, $\sigma_{xx}$, $\sigma_{yy}$) and strain increment components ($d\varepsilon_{xy}$, $d\varepsilon_{xx}$, $d\varepsilon_{yy}$) can be obtained to derive the geomechanical properties of the samples. The shear stress ratio is defined as $\tau_{xy}/\sigma_v$. The simple shear friction angle ($\phi_{ss}$) and dilation angle ($\psi$) can be calculated as

$$\tan\phi_{ss} = \frac{\tau_{xy}}{\sigma_v} \tag{3}$$

$$\tan\psi = -\frac{d\varepsilon_V}{d\gamma} \tag{4}$$

where $d\varepsilon_v$ and $d\gamma$ represent the volumetric strain and shear strain increment, respectively; and $-d\varepsilon_v/d\gamma$ denotes the dilation ratio of the sample during shear.

The orientations of major principal stress ($\alpha$) and major principal strain increment ($\beta$) relative to the horizontal direction can be expressed as

$$\alpha = \frac{1}{2}\arctan\left(\frac{2\tau_{xy}}{\sigma_{xx}-\sigma_{yy}}\right) \tag{5}$$

$$\beta = \frac{1}{2}\arctan\left(\frac{2d\varepsilon_{xy}}{d\varepsilon_{xx}-d\varepsilon_{yy}}\right) \tag{6}$$

### 2.2 Programs of DEM simulations

Seven soil samples were generated in the simulated tests, with five of them made of circular particles (D1 to D5), and two of them made of non-circular particles (A1 and A2). Table 2 summarizes the properties of the samples. The samples A1 and A2 were composed of non-circular particles with four different shapes as shown in Fig. 2(a). The non-circular particles were generated using CLUMP logic in PFC$^{2D}$. The main advantages of CLUMP logic are that the agglomerates created by this method act as a rigid body, so there is no relative

**Table 2** A summary of DEM sample profiles

| Numerical sample | Initial porosity, $n_0$ | Vertical stress, $\sigma_v$/kPa | Number of particles |
|---|---|---|---|
| Discs-1 (D1) | 0.12 | 200 | 935 |
| Discs-2 (D2) | 0.14 | 200 | 898 |
| Discs-3 (D3) | 0.16 | 200 | 873 |
| Discs-4 (D4) | 0.12 | 150 | 935 |
| Discs-5 (D5) | 0.12 | 100 | 935 |
| Agglomerates-1 (A1, sole C3) | 0.12 | 200 | 935 |
| Agglomerates-2 (A2, a random combination of C3-C6) | 0.12 | 200 | 935 (C3: 253; C4: 228; C5: 222; C6: 232) |

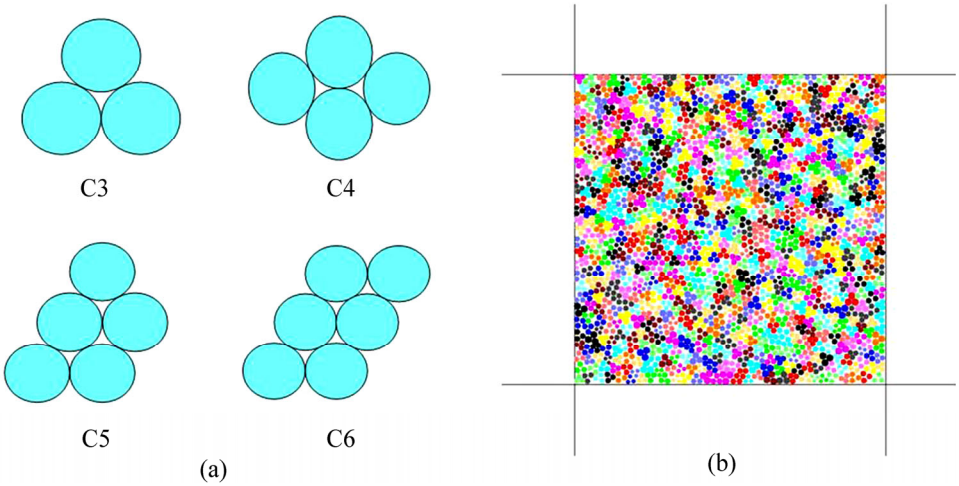


**Fig. 2** Numerical sampling: (a) Agglomerates created by CLUMP logic in PFC$^{2D}$; (b) Numerical model of A1 sample

movement between internal particles, and the calculation efficiency can be significantly improved by neglecting the interaction between internal particles. As shown in Fig. 2(a), C3 represents the agglomerates composed of three circular discs. The naming rules apply to C4–C6 as well. The A1 sample is generated using C3 agglomerates only, while the A2 sample is a random combination of C3 to C6. For the purpose of demonstration, the numerical model of A1 sample is shown in Fig. 2(b).

As listed in Table 2, the programs were divided into three simulation series to consider the effects of initial porosity, vertical stress and particle shape, respectively. In the first series, the same vertical stress was applied to samples of circular particles with different initial porosities (D1, D2 and D3). In the second series, different vertical stresses were applied to circular particle samples with the same initial porosity (D1, D4 and D5). The effects of particle shape were exclusively discussed in the third series with D1, A1 and A2 samples at the same vertical stress and initial porosity.

## 3 Macromechanical properties

### 3.1 Macroscopic response to simple shear

Figure 3 presents the behavior of the samples from the first simulation series with different initial porosities.

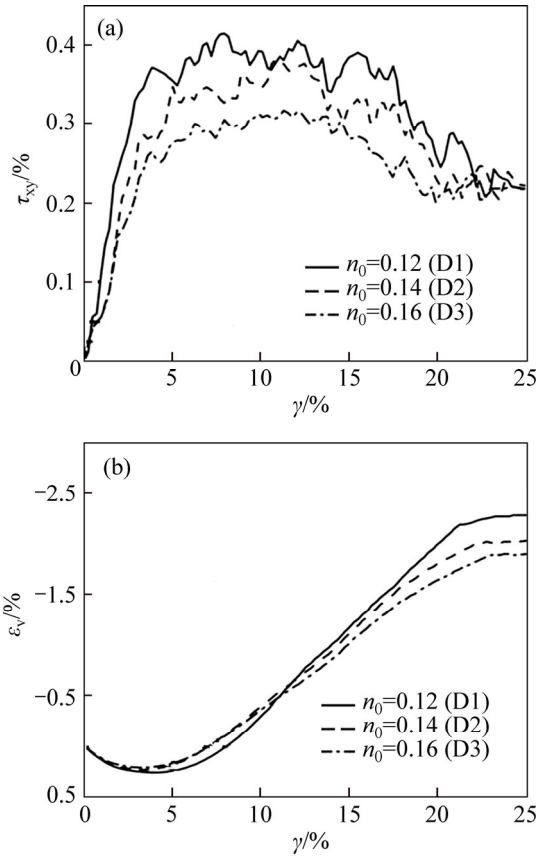


**Fig. 3** Macroscopic behavior of numerical samples with different initial porosities: (a) Shear stress ratio–shear strain curves; (b) Volumetric strain–shear strain curves

It is apparent from Fig. 3 that the dense granular assemblies exhibit typical volume dilation and strain-softening characteristics, which are very similar to those of dense sands under simple shear loading reported by THAY et al [1] and PRADHAN et al [13]. The stress−strain curves of all three samples can be distinctly divided to two stages: pre-peak and post-peak stages, as shown in Fig. 3(a). The sample reaches the peak shear stress ratio in the range of $\gamma$ from 8% to 12%. After peak, the shear stress ratio gradually decreases with increasing volume, as illustrated in Fig. 3(b). The shear stress ratio reaches to a residual value once the dilation stops at large shear strain, i.e. $\gamma$ = 25%. This value observed in the numerical modelling agrees well with the test results on dense sand samples as reported in Refs. [14−15].

As shown in Fig. 3, initial porosity ($n_0$) significantly affects the macroscopic behavior of the sample. The peak shear stress ratio decreases from 0.42 to 0.32 as $n_0$ increases from 0.12 to 0.16, whilst more significant volume dilation will exhibit with the decreasing of $n_0$, which can be seen in Fig. 3 (b) that under the same vertical pressure, the lower the initial porosity, the higher the maximum dilation rate, i.e. the maximum slope of the curve. The samples with different $n_0$ values reach the same residual shear strength at large shear strain as part of the critical state behavior of the material.

Figure 4 illustrates the shear behavior of the samples with same initial porosity under different vertical stresses. It can be seen from Fig. 4(a) that the peak shear strength is affected by vertical stress ($\sigma_v$). As $\sigma_v$ increases from 100 kPa to 200 kPa, the peak stress ratio increases from 0.32 to 0.42, whilst the residual shear strength at large shear strain is almost independent of $\sigma_v$. As illustrated in Fig. 4(b), at lower vertical stress levels, the samples contract less but swell more during shear. The figure also shows that the lower the vertical stress is, the earlier the swelling stage starts. During the dilation stage, the dilation curves in Fig. 4(b) are nearly parallel, which suggests that the samples dilate at almost the similar rate.

The shear behavior of the samples with different particle shapes with the same initial porosity and vertical stress is depicted in Fig. 5. As shown in Fig. 5(a), the particle shapes have great effect on the shear behavior of the samples. It can be seen from the figures that the higher the angularity of the particles is, the higher the peak shear strength and the sample dilation are. The highest peak shear stress ratio (0.59) was observed in the sample A2, which is about 40% higher than that (0.42) of D1 with circular particles. Figure 5(a) also shows that at the strain level 25%, the residual shear strength of the non-circular particle samples is significantly higher than that of the circular ones.

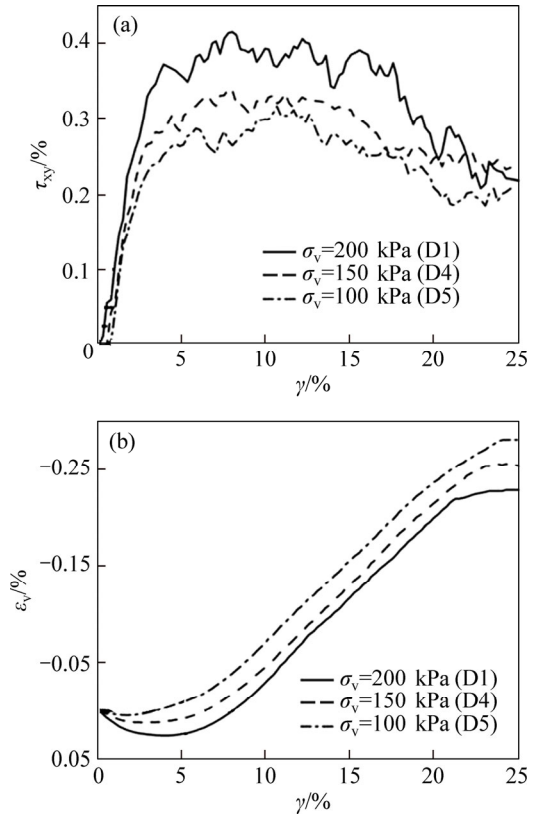


**Fig. 4** Macroscopic behavior of numerical samples under different vertical stresses: (a) Shear stress ratio–shear strain curves; (b) Volumetric strain–shear strain curves

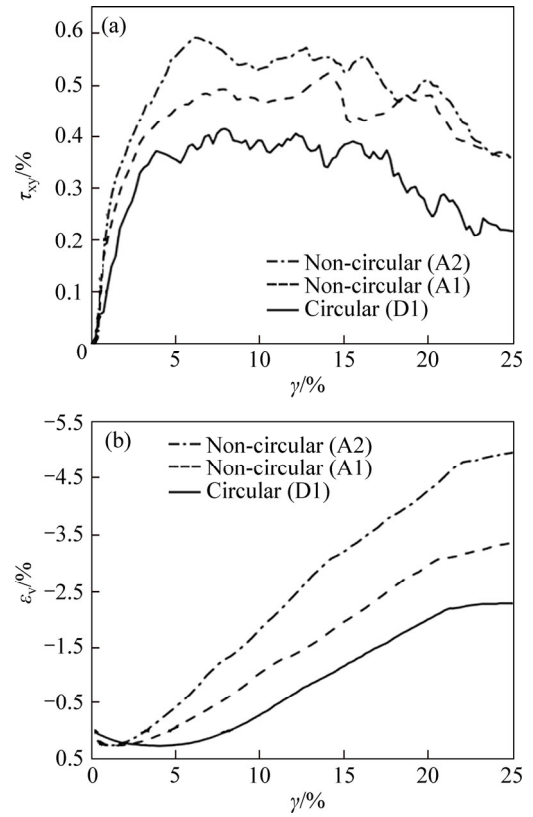


**Fig. 5** Macroscopic behavior of numerical samples with different particle shapes: (a) Shear stress ratio–shear strain curves; (b) Volumetric strain–shear strain curves

### 3.2 Non-coaxiality effect

The non-coaxiality effect induced by principal stress rotation in simple shear condition is studied in this section. The variation of major principal stress direction ($\alpha$) and major principal strain increment direction ($\beta$) with shear strain ($\gamma$) during shear is investigated. For brevity, only the results achieved from D1 circular and A2 non-circular particle samples are presented, as illustrated in Figs. 6(a) and (b), respectively. The non-coaxiality angle ($\Delta$) is defined as

$$\Delta = \beta - \alpha \tag{7}$$

It can be seen from Figs. 6(a) and (b) that the major principal stress and strain increment directions rotate quickly as shear strain increases and stabilize at lower shear strain values. Nearly 90% of the principal strain increment direction rotation finished at less than 3% shear strain and 90% of principal stress direction rotation finished at less than 5% shear strain. The rotation of principal stress direction lags behind the rotation of principal strain increment direction. Figure 6(c) describes the variation of $\alpha$ and $\beta$ of Toyoura sand from drained torsional simple shear test performed by PRADHAN et al [13]. The sand has initial porosity of 0.44 and was sheared at vertical stress of 98.1 kPa. It is shown that the overall trend of the variation of the non-coaxial curves of the simulated samples and tested sand agree well with each other.

Figure 6(d) compares the non-coaxiality angles of the samples A2, D1 and Toyoura sand. The figure shows that the non-coaxiality angle can be as large as nearly 25°, and the value decreases rapidly with the increment of shear strain. From the curves it can be seen that the change of non-coaxiality angle can be divided into three stages: the first stage is during the shear strain range of less than 5% when the orientation of the particles has been rearranged due to shear, which results in the rapid drop of non-coaxiality angle; the second stage is a "turbulence" stage or "transition" stage during the strain range of 5%–15% or even 20% when the non-coaxiality angle increases slightly, which results in the reach of peak strength; and the last stage is the "residual" stage when the non-coaxiality angle reduces to nearly zero at large strain levels, i.e. 20%, which indicates the residual stage of the samples. The curve of A2 in Fig. 6(d) shows that the non-coaxiality angle increases largest during the turbulence stage, which agrees with the observation of higher peak shear strength shown in Fig. 5. The figure also shows that the non-coaxiality angle of A2 sample reaches its residual stage at the largest strain level comparing with the samples of D1 and Toyoura sand.

### 3.3 Non-coaxial stress–dilatancy relationship

Based on the assumption of coaxiality between

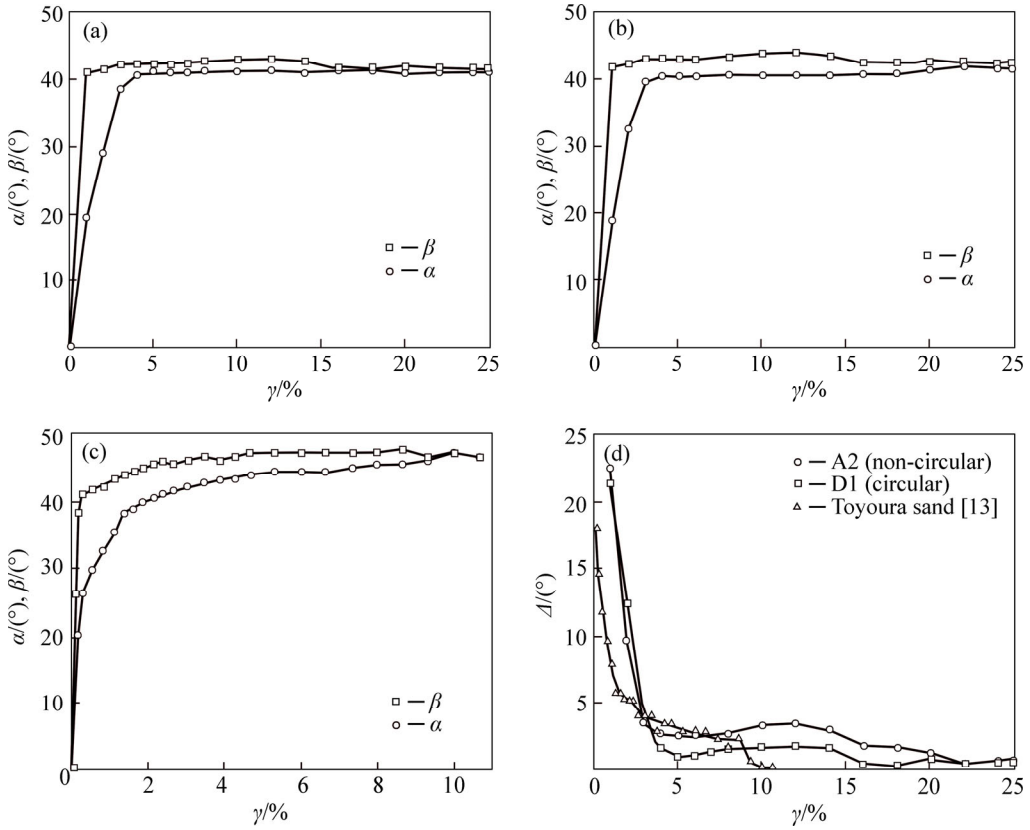


**Fig. 6** Non-coaxiality between $\alpha$ and $\beta$ during shear: (a) D1 sample (circular); (b) A2 sample (non-circular); (c) Toyoura sand [13]; (d) variation of non-coaxiality angle $\Delta$ with $\gamma$

principal stress and principal strain increment, ROWE [16] presented the classical stress–dilatancy relationship for granular soils under plane strain condition, which can be expressed as

$$\sin\phi_{\mathrm{ps}}=\frac{\sin\phi_{\mathrm{cr}}+\sin\psi}{1+\sin\phi_{\mathrm{cr}}\sin\psi} \tag{8}$$

where $\phi_{\mathrm{ps}}$ is the plane strain friction angle, and $\phi_{\mathrm{cr}}$ is the critical state friction angle. The plane strain friction angle can be derived from simple shear friction angle ($\phi_{\mathrm{ss}}$) using the equation proposed by DAVIS [17]:

$$\sin\phi_{\mathrm{ps}}=\frac{\tan\phi_{\mathrm{ss}}}{\tan\phi_{\mathrm{ss}}\sin\psi+\cos\psi} \tag{9}$$

By rearranging Eqs. (8) and (9), we have

$$\tan\phi_{\mathrm{ss}}=\frac{\sin\phi_{\mathrm{cr}}+\sin\psi}{\cos\psi} \tag{10}$$

At residual state, $\psi$ is generally assumed to be 0. Then, Eq. (10) becomes

$$\tan\phi_{\mathrm{ss}}^{\mathrm{r}}=\sin\phi_{\mathrm{cr}} \tag{11}$$

where $\phi_{\mathrm{ss}}^{\mathrm{r}}$ represents the residual friction angle in simple shear.

Substituting Eq. (11) into Eq. (10) yields

$$\tan\phi_{\mathrm{ss}}=\frac{\tan\phi_{\mathrm{ss}}^{\mathrm{r}}+\sin\psi}{\cos\psi} \tag{12}$$

Equation (12) is the ROWE-DAVIS stress–dilatancy equation for simple shear condition without considering non-coaxiality. Figures 7(a) and (b) describe the stress and strain increment states by Mohr's circles for coaxial condition, while Fig. 7(c) illustrates the superimposed Mohr's circles describing the non-coaxiality effect, in which the stress circle and the strain increment circle are coincided. As described above, non-coaxiality effect cannot be neglected during shear, especially before the peak state. As shown in Fig. 7(c), the dilation angle will reduce from $\psi$ to $\psi$–$2\Delta$ when non-coaxiality effect is considered. Therefore, Eq. (12) is extended to account for non-coaxiality effect:

$$\tan\phi_{\mathrm{ss}}=\frac{\tan\phi_{\mathrm{ss}}^{\mathrm{r}}+\sin\left(\psi-2\Delta\right)}{\cos\left(\psi-2\Delta\right)} \tag{13}$$

At peak state, Eq. (13) can be rewritten as

$$\tan\phi_{\mathrm{ss}}^{\mathrm{p}}=\frac{\tan\phi_{\mathrm{ss}}^{\mathrm{r}}+\sin\left(\psi_{\mathrm{p}}-2\Delta_{\mathrm{p}}\right)}{\cos\left(\psi_{\mathrm{p}}-2\Delta_{\mathrm{p}}\right)} \tag{14}$$

where $\phi_{\mathrm{ss}}^{\mathrm{p}}$ is the peak friction angle of the samples in simple shear, and $\psi_{\mathrm{p}}$ and $\Delta_{\mathrm{p}}$ are the dilation angle and non-coaxiality angle at peak state, respectively.

The numerical results of the samples are listed in Table 3, and some published data are used to validate the proposed non-coaxial stress–dilatancy relationship in

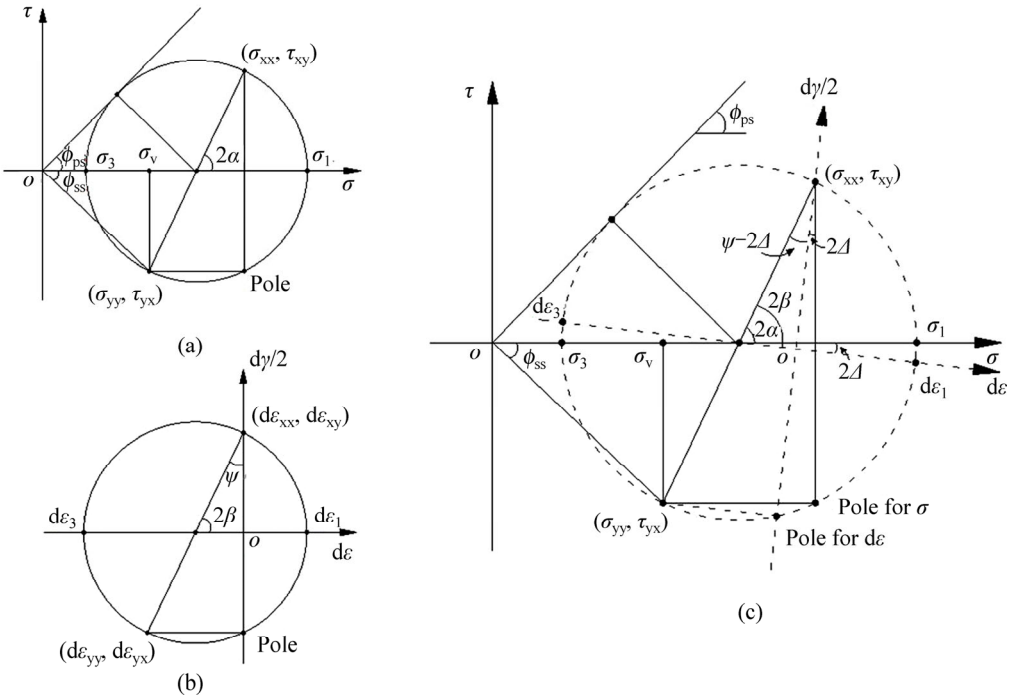


**Fig. 7** Description of non-coaxiality effect by Mohr's circles: (a) Stress circle; (b) Strain increment circle; (c) Superimposed circles of stress and strain increment considering non-coaxiality

**Table 3** Analyses of non-coaxial stress-dilatancy relationship

| Sample | $\phi_{ss}^{r}$/(°) | $\psi_p$/(°) | $\Delta_p$/(°) | $\phi_{ss}^{p}$/(°) | | | Deviation/% | |
|---|---|---|---|---|---|---|---|---|
| | | | | Simulated/tested | Eq. (12) | Eq. (14) | Eq. (12) | Eq. (14) |
| D1 (Circular) | 12.4 | 13.2 | 1.5 | 22.8 | 24.7 | 22.0 | 8.3 | -3.5 |
| D2 (Circular) | 12.4 | 11.3 | 1.5 | 20.8 | 23.0 | 20.2 | 10.6 | -2.9 |
| D3 (Circular) | 12.4 | 9.2 | 1.2 | 17.7 | 21.1 | 18.8 | 19.2 | 6.2 |
| D4 (Circular) | 12.4 | 10.8 | 1.5 | 18.8 | 22.5 | 19.8 | 19.7 | 5.3 |
| D5 (Circular) | 11.3 | 10.6 | 1.2 | 17.7 | 21.3 | 19.1 | 20.3 | 7.9 |
| A1 (Non-circular) | 19.3 | 14.5 | 2.2 | 27.5 | 31.8 | 28.1 | 15.6 | 2.2 |
| A2 (Non-circular) | 20.8 | 18.1 | 2.5 | 30.5 | 36.0 | 31.9 | 18.0 | 4.6 |
| DEM ellipses [18] ($n_0$ = 0.175, $\sigma_v$ = 200 kPa) | 24.2 | 7.7 | 1.5 | 28.8 | 30.5 | 28.1 | 5.9 | -2.4 |
| DEM discs [11] ($n_0$ = 0.21, $\sigma_v$ = 130 kPa) | 20.7 | 7.5 | 2.5 | 21.7 | 27.2 | 22.9 | 25.3 | 5.5 |
| DEM discs [9] (Dense*, $\sigma_v$ = 10 MPa, $K_0$ = 2.0) | 15.1 | 15.5 | 5.0 | 23.3 | 29.1 | 20.2 | 24.9 | -13.3 |
| Photoelastic rods [19] ($n_0$ = 0.18, $\sigma_v$ = 130 kPa) | 22.0 | 14.8 | 5.0 | 27.7 | 34.3 | 26.1 | 23.8 | -5.8 |
| Toyoura sand [13] ($n_0$ = 0.41, $\sigma_v$ = 98.1 kPa) | 34.7 | 12.6 | 3.5 | 35.5 | 43.0 | 38.5 | 21.1 | 8.5 |
| Leighton Buzzard sand [20] ($n_0$ = 0.35, $\sigma_v$ = 14 kPa) | 41.2 | 9.2 | 2.0 | 45.0 | 46.4 | 44.2 | 3.1 | -1.8 |

Note: No information of initial porosity was referred in Ref. [9], and $K_0$ is the ratio of initial horizontal stress to vertical stress.

Eq. (14). The data cover a large range of materials, such as DEM simulated circular [9, 11], non-circular particles [18] and photoelastic rods [19], and test results from Toyoura sand [13] and Leighton Buzzard sand (LB sand) [20]. In Table 3, the simulated/tested data of peak simple shear friction angle $\phi_{ss}^{p}$ are compared with the values calculated from Eqs. (12) and (14). It should be noted that the data reported by SHI et al [18] in Table 3 are from simulated direct shear tests using DEM on planar elliptical particles with an aspect ratio of 1.4. It is

normally accepted that the deformation pattern within the shear band under direct shear can be considered a simple shear mode [21]. It can be seen that using the results from direct shear test also gives good estimation of peak friction angle of soils in simple shear.

It can be found in Table 3 that the non-coaxiality angle of the selected materials ranges from 1.2° to 5° at peak state, which is considerably high compared with the degrees of peak friction angle (4% to 20% of the peak friction angle). The calculated values by Eq. (12) with no consideration of non-coaxiality will maximally overestimate the simulated/tested values up to 25%. However, when Eq. (14) is adopted, the absolute deviations are reduced to under 15%, and 90% of the estimated values with an absolute deviation less than 10%. It can be further seen in Fig. 8 that Eq. (14) better describes the peak shear strength of dense granular assemblies under simple shear incorporating non-coaxiality.

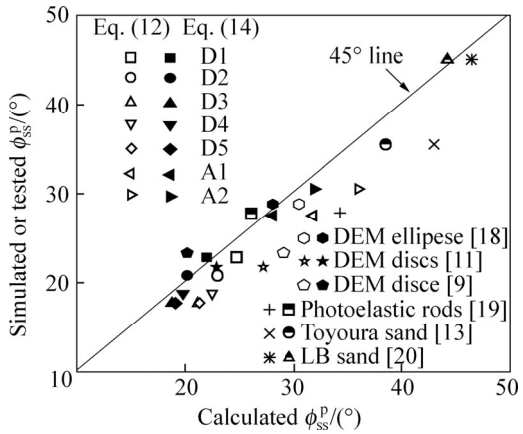


**Fig. 8** Validation of non-coaxial stress-dilatancy relationship

## 4 Stress-induced anisotropy

In this section, the evolution of fabric anisotropy, which can be described using anisotropy of contact normal [22−23], and contact force anisotropy subjected to principal stress rotation are investigated. For brevity, only the results from D1 and A2 samples, which represent the circular and non-circular particle samples, are discussed in detail. The frequency distribution functions suggested by ROTHENBURG and BATHURST [24] are used to quantitatively describe the anisotropic distributions of contact normal and contact force:

$$E(\theta)=\frac{1}{2\pi}\left[1+a\cos\left(2\left(\theta-\theta_{\mathrm{a}}\right)\right)\right] \tag{15}$$

$$f_{\mathrm{n}}(\theta)=f_0\left[1+a_{\mathrm{n}}\cos\left(2\left(\theta-\theta_{\mathrm{n}}\right)\right)\right] \tag{16}$$

$$f_{\mathrm{t}}(\theta)=-f_0 a_{\mathrm{t}}\sin\left(2\left(\theta-\theta_{\mathrm{t}}\right)\right) \tag{17}$$

where $E(\theta)$, $f_{\mathrm{n}}(\theta)$ and $f_{\mathrm{t}}(\theta)$ represent the orientation distributions of contact normal, contact normal force and contact tangential force, respectively; $a$, $a_{\mathrm{n}}$ and $a_{\mathrm{t}}$ are the coefficients of contact normal anisotropy, normal contact force anisotropy and tangential contact force anisotropy, respectively; $\theta_{\mathrm{a}}$, $\theta_{\mathrm{n}}$ and $\theta_{\mathrm{t}}$ are the principal directions of contact normal anisotropy, contact normal force anisotropy, and contact tangential force anisotropy respectively; $f_0$ is the average value of contact normal force over all contacts in the assembly.

Figures 9(a)−(c) illustrate the orientation distributions of contact normal and contact force of D1 sample at initial state ($\gamma$=0), peak state ($\gamma$=8%) and residual state ($\gamma$=25%), respectively. The solid line in Fig. 9 represents the DEM results and the dashed line denotes the Fourier approximation given by Eqs. (15)–(17). The nephograms of interparticle contact force chain are also demonstrated in Fig. 9. Figure 9 shows that at the initial state, the contact normal and contact force distributions are uniform as the sample was isotropically consolidated and the contact force between the particles acted dominantly on normal direction. At peak state, the dominant directions of contact normal and normal contact force anisotropies rotate, to an angle of 32° to 34° and remain almost unchanged till residual state. Whilst the anisotropic direction of tangential contact force rotated to an angle of 27.1° at peak state and slightly increased to 29.4° at residual state. The coefficients of anisotropies of contact normal and contact forces ($a$, $a_{\mathrm{n}}$, $a_{\mathrm{t}}$) increased dramatically from nearly zero at initial stage to (0.31, 0.42, 0.13) at peak state and reduced to (0.24, 0.31, 0.11) at residual state. This suggests that from peak to residual state, the major directions of contact normal and contact force anisotropies remain almost unchanged, whilst the extent of these anisotropies reduces.

Figure 10(a) describes the variation of anisotropic coefficients ($a$, $a_{\mathrm{n}}$, $a_{\mathrm{t}}$) of D1 sample with the shear strain ($\gamma$) during shear. It can be seen from Fig. 10(a) that the evolution of fabric and contact force anisotropies follows the same trend with the development of the shear resistance. At the beginning of shear, anisotropic coefficients increase with shear strain, and reach their maximum values at the peak shear stress ratio. Thereafter, anisotropic coefficients gradually decrease as the sample reaches post-peak strain softening stage. It should be noted that, among $a$, $a_{\mathrm{n}}$, $a_{\mathrm{t}}$, $a_{\mathrm{n}}$ is significantly larger than $a$ or $a_{\mathrm{t}}$ at all strain levels. Therefore, it is obvious that the macroscopic shear strengthening of a granular assembly is primarily caused by the development of contact normal force anisotropy, which supports the findings from direct shear simulations reported by WANG et al [25] and SHI et al [18].

Figure 10(b) depicts the variation of the principal directions of contact normal anisotropy, normal and

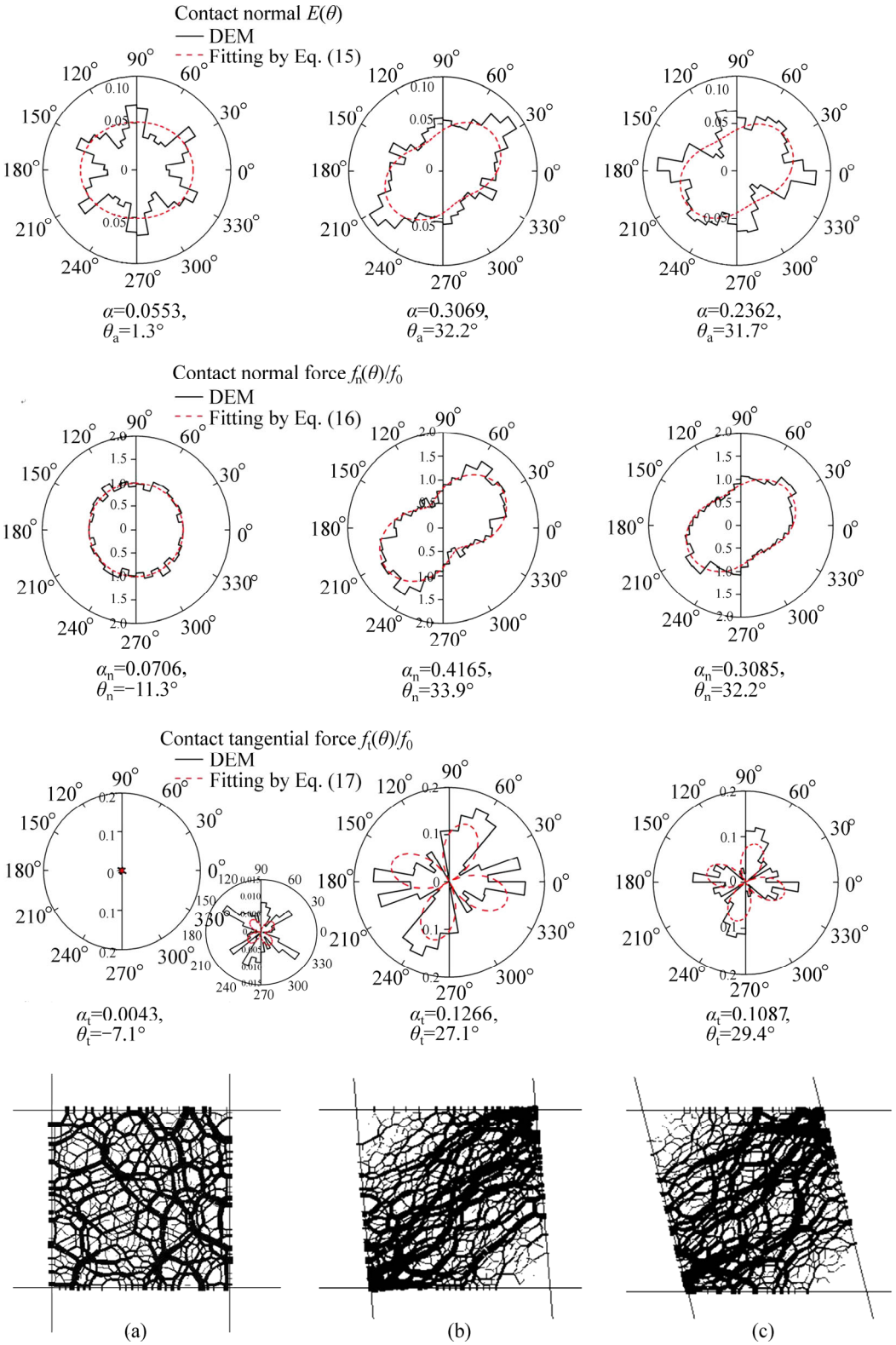


**Fig. 9** Evolution of fabric and contact force anisotropies of D1 sample: (a) $\gamma$=0 (initial state); (b) $\gamma$=8% (peak state); (c) $\gamma$=25% (residual state)

tangential contact force anisotropies ($\theta_a$, $\theta_n$, $\theta_t$) with the shear strain ($\gamma$). To explore the potential macro–micro relationships, the variation of major principal stress direction ($\alpha$) with $\gamma$ is plotted in Fig. 10(b) as well. As illustrated in Fig. 10(b), the rotation of anisotropic directions of contact normal and contact forces nearly finishes at the peak state, and gradually stabilities after that. The rotation of the principal directions of contact normal anisotropy ($\theta_a$) and normal contact force anisotropy ($\theta_n$) follows almost the same curve as shear

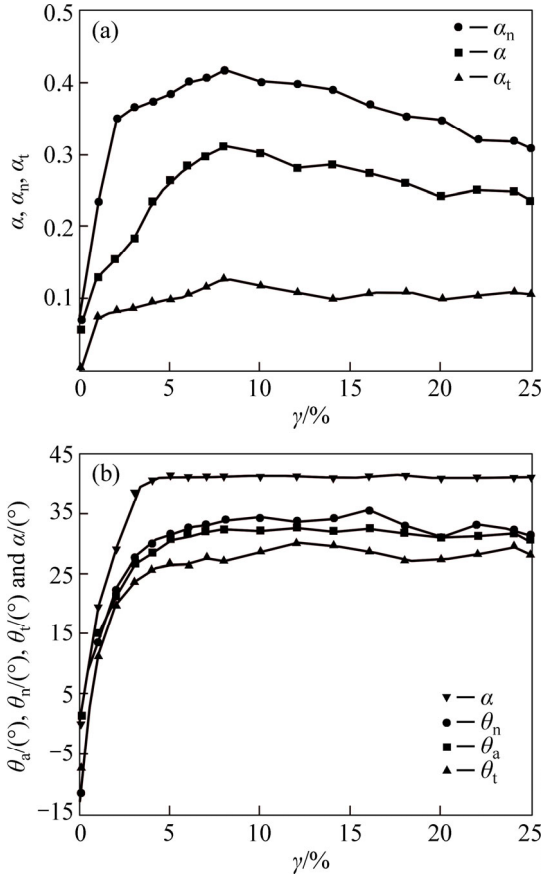


**Fig. 10** Variation of fabric and contact force anisotropies with shear strain of D1 sample: (a) Anisotropic coefficients ($a$, $a_n$, $a_t$); (b) Principal direction angles of anisotropies ($\theta_a$, $\theta_n$, $\theta_t$) and $\alpha$

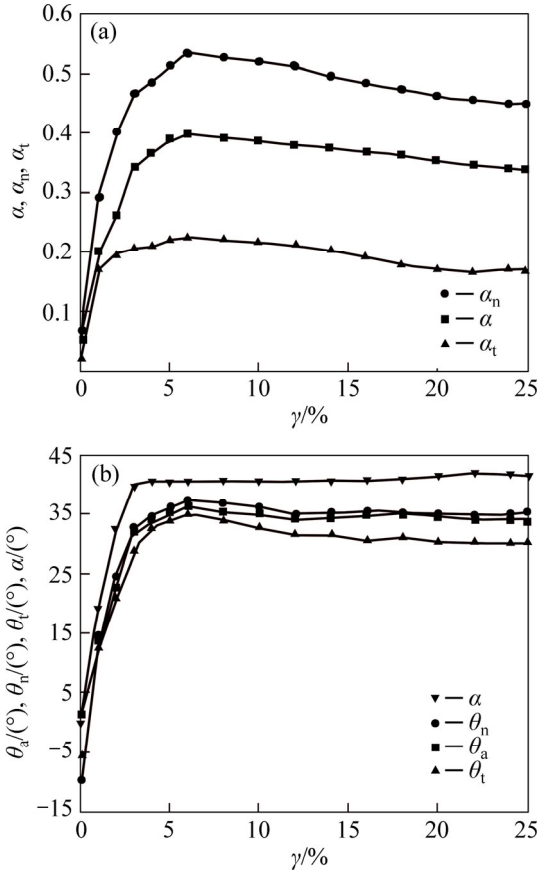


**Fig. 11** Variation of fabric and contact force anisotropies with shear strain of A2 sample (non-circular): (a) Anisotropic coefficients ($a$, $a_n$, $a_t$); (b) Principal direction angles of anisotropies ($\theta_a$, $\theta_n$, $\theta_t$) and $\alpha$

strain increases, which suggests that normal contact force rotates with the direction of the contacts or vice versa. The principal direction of contact tangential force anisotropy ($\theta_t$) is slightly less than that of $\theta_a$ and $\theta_n$.

Figure 10(b) also shows a clear fabric hysteresis effect during shear, which suggests that the orientation of fabric (contact normal) anisotropy ($\theta_a$) lags behind the evolution of the major principal stress direction ($\alpha$). It can be seen that: 1) the direction of major principal stress ($\alpha$) stabilized at relatively lower strain levels (5%) comparing to the principal direction of fabric anisotropy ($\theta_a$) which stabilized at the strain level of 8%; and 2) the maximum angle of fabric anisotropy ($\theta_a$) is almost 10° or 25% less than that of the major principal stress ($\alpha$) during the steady state. This phenomenon has not been explored in direct shear simulations conducted by WANG et al [25] and SHI et al [18]. This discrepancy is mainly due to the significant non-uniform stress and deformation fields within the direct shear sample.

Figure 11 describes the evolution of fabric and contact force anisotropies of the non-circular particle sample A2. It can be seen from Figs. 10 and 11 that the overall trends of the evolution of the parameters with strain of the two samples are similar, but the maximum values of anisotropic coefficients ($a$, $a_n$, $a_t$) increase from (0.31, 0.42, 0.13) for D1 to (0.4, 0.53, 0.22) for A2, which indicates that the higher the angularity of particles, the higher the anisotropy. Among the three coefficients, $a_n$ is still the largest as seen in the results of D1 in Fig. 10(a), which supports the claim that the development of shear resistance is mainly affected by the evolution of the anisotropy of the contact normal force rather than the shape of the particles.

Figure 11(b) shows that the fabric hysteresis effect also exists for samples with non-circular particles. The angle of the major principal stress ($\alpha$) is greater than that of fabric anisotropy ($\theta_a$) during the steady state, but is only about 5° greater, which is only half of the value observed in D1. This may suggest that the hysteresis effect is less in samples with angular particles. By comparing Figs. 10(b) and 11(b), we can see that the maximum values of the major principal stress direction ($\alpha$) of the two samples are almost the same, in the range of 41°. The decrease of hysteresis effect observed in the sample with non-circular particles is mainly due to the increase of the angle of fabric anisotropy.

## 5 Stress–force–fabric relationship

Since the pioneering work by ODA [26], many studies have been carried out on the topic of stress–force–fabric relationship for granular materials [27−28]. Nevertheless, the previous studies mainly focus on the proportional loading condition, and few attentions have been paid to the stress condition involving principal stress rotation. LI and YU [29] investigated the stress–force–fabric relationship for non-proportional loading, and the authors suggested that a more general expression should be proposed for the stress–force–fabric relationship when the principal directions of stress and fabric anisotropy are non-coaxial. In this study, an empirical stress–force–fabric relationship incorporating the fabric hysteresis effect induced by principal stress rotation will be discussed.

Based on DEM simulations of biaxial tests, ROTHENBURG and BATHURST [24] presented a stress–force–fabric relationship for plane strain condition subjected to proportional loading expressed as

$$\sin\phi_{\mathrm{ps}} = \frac{1}{2}(a + a_{\mathrm{n}} + a_{\mathrm{t}}) \tag{18}$$

where $\sin\phi_{\mathrm{ps}}$ is the mobilized shear strength of the sample.

As mentioned before, non-coaxiality effect should be considered when the stress–dilatancy behavior is analyzed under the condition of principal stress rotation. Considering the reduction of dilation angle from $\psi$ to $\psi$–2$\Delta$, an extended form of DAVIS equation (Eq. (9)) is proposed to calculate the mobilized shear strength ($\sin\phi_{\mathrm{ps}}$) to consider non-coaxiality effect by replacing $\psi$ in Eq. (9) with $\psi$–2$\Delta$:

$$\sin\phi_{\mathrm{ps}} = \frac{\tan\phi_{\mathrm{ss}}}{\tan\phi_{\mathrm{ss}}\sin(\psi - 2\Delta) + \cos(\psi - 2\Delta)} \tag{19}$$

With respect to the fabric hysteresis effect, the angle of fabric hysteresis ($\delta_{\mathrm{a}}$) can be defined as

$$\delta_{\mathrm{a}} = \alpha - \theta_{\mathrm{a}} \tag{20}$$

A new stress–force–fabric equation based on Eq. (18) to incorporate $\delta_{\mathrm{a}}$ can be expressed as

$$\sin\phi_{\mathrm{ps}} = \frac{1}{2}\left[a\cos(2\delta_{\mathrm{a}}) + \sqrt{(a_{\mathrm{n}} + a_{\mathrm{t}})^2 - a^2\sin^2(2\delta_{\mathrm{a}})}\right] \tag{21}$$

When $\delta_{\mathrm{a}}$=0, Eq. (21) reduces to Eq. (18) under proportional loading.

Figure 12 compares the computed results of $\sin\phi_{\mathrm{ps}}$ using Eqs. (18)–(21) on circular (D1) and non-circular (A2) particle samples. It is illustrated in Fig. 12 that yet there exist some deviations at large shear strain level (i.e. $\gamma$≥20%) due to strain localization taking place within the samples and the calculated values of $\sin\phi_{\mathrm{ps}}$ given by Eq. (21) is very close to the simulated mobilized shear strength achieved using Eq. (19), while those calculated with ROTHENBURG and BATHURST's equation (Eq. (18)) give higher mobilized shear strength due to the ignorance of the fabric hysteresis effect. It clearly indicates that the deviation between the principal directions of stress and fabric anisotropy will lead to shear strength reduction of granular samples, which favorably agrees with the findings reported by QIAN et al [11].

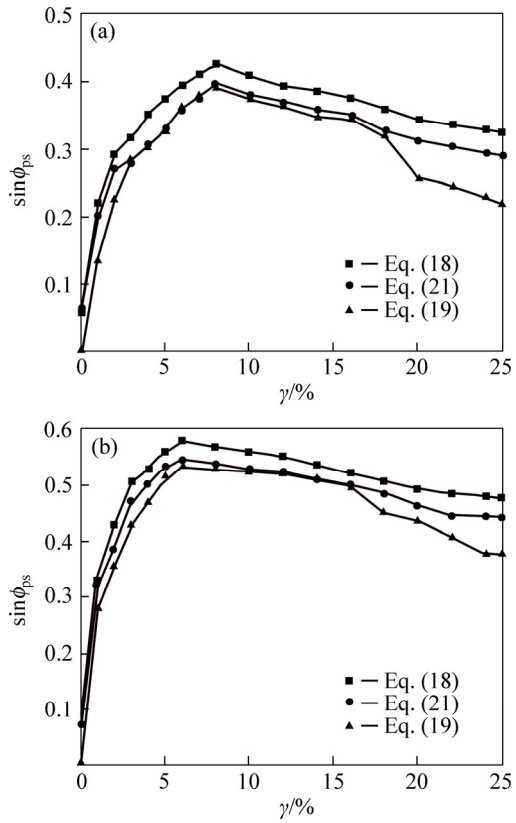


**Fig. 12** Validation of stress–force–fabric relationship: (a) D1 sample (circular); (b) A2 sample (non-circular)

## 6 Conclusions

1) Some of the major macroscopic behaviors of dense granular assemblies under simple shear can be successfully captured in DEM simulations, such as dilation and strain-softening. Particle shape will affect both macro and microscopic behaviors of numerical samples. For circular particles, the critical state behavior is observed to be independent of initial porosity and vertical stress. Higher peak and residual friction angles have been observed in non-circular particle samples due to the higher angularity of the particles and the anisotropic coefficients.

2) Non-coaxiality between the directions of principal stress and principal strain increment has been observed in numerical samples, which agrees with the finding from Toyoura sand. The non-coaxiality angle is

slightly affected by the shape of the particles but mainly by the strain level. Non-coaxiality is the largest at the start of the shear then reduces with the shear strain and almost diminishes as the sample reaches the residual state.

3) The non-coaxiality effect greatly affects the shear behavior of the assemblies. Using the results from the simulated and published data, an equation (Eq. (14)) is proposed to consider the non-coaxiality effect in describing the stress–dilatancy behavior of the assemblies. The proposed equation better describes the peak friction angles of granular materials than the current ROWE-DAVIS model.

4) During the course of simple shear, the evolution tendencies of fabric and contact force anisotropies are in good agreement with the development of shear resistance. The maximum degrees of fabric and contact force anisotropies occur when shear stress ratio reaches its peak value. Nevertheless, no coincidence has been observed between the rotation of principal stress direction and the orientation of fabric anisotropy during shear.

5) Fabric hysteresis effect has been observed in the simulations. The fabric hysteresis effect is less in samples with angular particles. The decrease of hysteresis effect observed in the sample with non-circular particles is considered due to the increase of the angle of fabric anisotropy. An equation (Eq. (21)) is proposed to describe the fabric hysteresis effect on stress–force–fabric relationship. The proposed model well captures the stress–force–fabric relationship of the samples with circular and non-circular particles.

## References


[1] THAY S, LIKITLERSUANG S, PIPATPONGSA T. Monotonic and cyclic behavior of Chiang Mai sand under simple shear mode [J]. Geotechnical and Geological Engineering, 2013, 31(1): 67−82.

[2] KJELLMAN W. Testing the shear strength of clay in Sweden [J]. Geotechnique, 1951, 2(3): 225−232.

[3] MORTEZAIE A R, VUCETIC M. Effect of frequency and vertical stress on cyclic degradation and pore water pressure in clay in the NGI simple shear device [J]. Journal of Geotechnical and Geoenvironmental Engineering, 2013, 139(10): 1727−1737.

[4] RUTHERFORD C J, BISCONTIN G. Development of a multidirectional simple shear testing device [J]. Geotechnical Testing Journal, 2013, 36(6): 1−9.

[5] ESELLER-BAYAT E, GOKVER S, YEGIAN M K, ORTAKCI E, ALSHAWABKEH A. Design and application of simple shear liquefaction box [J]. Geotechnical Testing Journal, 2013, 36(3): 1−9.

[6] ODA M, KONISHI J. Microscopic deformation mechanism of granular material in simple shear [J]. Soils and Foundations, 1974, 14(4): 25−38.

[7] MATSUOKA H. A microscopic study on shear mechanism of granular materials [J]. Soils and Foundations, 1974, 14(1): 29−43.

[8] LIU Si-hong, LU Ting-hao. Microscopic shear mechanism of granular materials in simple shear by DEM [J]. Chinese Journal of Geotechnical Engineering, 2000, 22(5): 608−611.

[9] THORNTON C, ZHANG L. A numerical examination of shear banding and simple shear non-coaxial flow rules [J]. Philosophical Magazine, 2006, 86(21/22): 3425−3452.

[10] SHEN C K, O'SULLIVAN C, JARDINE R J. A micromechanical investigation of drained simple shear tests [C]// International Symposium on Deformation Characteristics of Geomaterials, Seoul, Korea: IOS Press, 2011: 314−321.

[11] QIAN Jian-gu, YOU Zi-pei, HUANG Mao-song. Anisotropic characteristics of granular materials under simple shear [J]. Journal of Central South University, 2013, 20(8): 2275−2284.

[12] ZHOU Jian, SHI Dan-da, JIA Min-cai. Numerical simulation of mechanical response on sand under monotonic loading by particle flow code [J]. Journal of Tongji University, 2007, 35(10): 1299−1304. (in Chinese)

[13] PRADHAN T B S, TATSUOKA F, HORII N. Simple shear testing on sand in a torsional shear apparatus [J]. Soils and Foundations, 1988, 28(2): 95−112.

[14] VERDUGO R, ISHIHARA K. The steady state of sandy soils [J]. Soils and Foundations, 1996, 36(2): 81−91.

[15] ATKINSON J, LAU W H W, POWELL J J M. Measurement of soil strength in simple shear tests [J]. Canadian Geotechnical Journal, 1991, 28(3): 255−262.

[16] ROWE P W. The stress dilatancy relation for static equilibrium of an assembly of particles in contact [J]. Proceedings of the Royal Society of London. Series A, Mathematical and Physical Sciences, 1962, 269(1239): 500−527.

[17] DAVIS E H. Theories of plasticity and the failure of soil masses [M]// LEE K I, ed. Soil Mechanics: Selected Topics. London: Butterworth, 1968: 341−380.

[18] SHI Dan-da, ZHOU Jian, LIU Wen-bai, DENG Yi-bing. Exploring macro- and micro-scale responses of sand in direct shear tests by numerical simulations using non-circular particles [J]. Chinese Journal of Geotechnical Engineering, 2010, 32(10): 1557−1565. (in Chinese)

[19] ODA M, KONISHI J. Rotation of principal stresses in granular material during simple shear [J]. Soils and Foundations, 1974, 14(4): 39−53.

[20] STROUD M A. The behavior of sand at low stress levels in the simple shear apparatus [D]. Cambridge: University of Cambridge, 1971.

[21] SHIBUYA S, MITACHI T, TAMATE S. Interpretation of direct shear box testing of sands as quasi-simple shear [J]. Geotechnique, 1997, 47(4): 769−790.

[22] YANG Z X, LI X S, YANG J. Quantifying and modeling fabric anisotropy of granular soils [J]. Geotechnique, 2008, 58(4): 237−248.

[23] SITHARAM T G, VINOD J S, RAVISHANKAR B V. Post-liquefaction undrained monotonic behavior of sands: experiments and DEM simulations [J]. Geotechnique, 2009, 59(9): 739−749.

[24] ROTHENBURG L, BATHURST R J. Analytical study of induced anisotropy in idealized granular materials [J]. Geotechnique, 1989, 39(4): 601−614.

[25] WANG J, DOVE J E, GUTIERREZ M S. Discrete-continuum analysis of shear banding in the direct shear test [J]. Geotechnique, 2007, 57(6): 513−526.

[26] ODA M. Initial fabrics and their relations to mechanical properties of granular material [J]. Soils and Foundations, 1972, 12(1): 17−36.

[27] HOSSEININIA E S. Stress-force-fabric relationship for planar granular materials [J]. Geotechnique, 2013, 63(10): 830−841.

[28] LI X, YU H S. On the stress-force-fabric relationship for granular materials [J]. International Journal of Solids and Structures, 2013, 50(9): 1285−1302.

[29] LI X, YU H S. Applicability of stress-force-fabric relationship for non-proportional loading [J]. Computers and Structures, 2011, 89(11/12): 1094−1102.


**(Edited by DENG Lü-xiang)**